RESEARCH ARTICLE

Rising Stars

NANO · MICRO small

www.small-journal.com

Real-Time, In Situ Imaging of Macrophages via Phase-Change Peptide Nanoemulsions

*Inhye Kim, Jacob C. Elliott, Atip Lawanprasert, Grace M. Wood, Julianna C. Simon, and Scott H. Medina**

Macrophages are specialized phagocytes that play central roles in immunity and tissue repair. Their diverse functionalities have led to an evolution of new allogenic and autologous macrophage products. However, realizing the full therapeutic potential of these cell-based therapies requires development of imaging technologies that can track immune cell migration within tissues in real-time. Such innovations will not only inform treatment regimens and empower interpretation of therapeutic outcomes but also enable prediction and early intervention during adverse events. Here, phase-changing nanoemulsion contrast agents are reported that permit real-time, continuous, and high-fidelity ultrasound imaging of macrophages in situ. Using a de novo designed peptide emulsifier, liquid perfluorocarbon nanoemulsions are prepared and show that rational control over interfacial peptide assembly affords formulations with tunable acoustic sensitivity, macrophage internalization, and in cellulo stability. Imaging experiments demonstrate that emulsion-loaded macrophages can be readily visualized using standard diagnostic B-mode and Doppler ultrasound modalities. This allows on-demand and long-term tracking of macrophages within porcine coronary arteries, as an exemplary model. The results demonstrate that this platform is poised to open new opportunities for non-invasive, contrast-enhanced imaging of cell-based immunotherapies in tissues, while leveraging the low-cost, portable, and safe nature of diagnostic ultrasound.

1. Introduction

Macrophages are phagocytic cells that play key roles in innate and adaptive immunity.[1,2] They are important cellular mediators of wound healing[3] and tissue regeneration,[4] and contribute to inflammatory-linked diseases that include diabetes,[5] atherosclerosis,[6] and rheumatoid arthritis.[7] These varied effector functions have spurred interest in developing modified and engineered macrophage cell therapies, particularly for oncology.[8,9] However, like all cell-based therapies, variable biodistribution profiles and tissue migration patterns can lead to heterogenous therapeutic responses and increase the risk of unwanted side effects.[10] Accordingly, technologies that enable real-time and long-term imaging of macrophages would allow clinicians and scientists to monitor tissue distribution in situ to inform treatment approaches, predict and avoid off-target toxicities, and ultimately enhance our understanding of the dynamic behavior of these cells.

Toward this goal, fluorescence,[11] magnetic resonance,[12] and positron emission tomography[13] imaging modalities have been explored for macrophage monitoring. While these methods enable exquisite visual resolution, they have several notable drawbacks. They often require expensive instrumentation and highly trained technicians, suffer from limited tissue depth, or are unable to provide real-time and continuous monitoring of cell motion. Ultrasound (US) imaging is an attractive alternative as it is inexpensive, portable, radiation-free, and provides real-time acquisition in a non-invasive manner with excellent penetration depth and spatial resolution when paired with microbubble acoustic contrast agents.[14,15] However, traditional bubble-based agents used for ultrasonography cannot be readily coupled to macrophages due to low uptake efficiency,[16] and have short persistence time in circulation due to gas diffusion into blood.[17]

Here, we report liquid phase-changing nanoemulsions that are readily internalized into macrophages and undergo a US directed liquid-to-gas phase transition to convert into echogenic microbubbles in situ. This enables on-demand, real-time, and continuous acoustic imaging of macrophages in tissues with high spatiotemporal resolution. Importantly, we show that modulating the interfacial assembly of the stabilizing emulsifier allows

I. Kim, A. Lawanprasert, J. C. Simon, S. H. Medina
Department of Biomedical Engineering
Pennsylvania State University
University Park, PA 16802-4400, USA
E-mail: shm126@psu.edu
J. C. Elliott, G. M. Wood, J. C. Simon
Graduate Program in Acoustics
Pennsylvania State University
University Park, PA 16802-4400, USA
S. H. Medina
Huck Institutes of the Life Sciences
Pennsylvania State University
University Park, PA 16802-4400, USA

The ORCID identification number(s) for the author(s) of this article can be found under https://doi.org/10.1002/smll.202301673

DOI: 10.1002/smll.202301673

us to produce particles with varied surface morphologies and, as a result, tunable acoustic properties and in cellulo stability. These findings highlight the potential of this platform to open new imaging-guided approaches to improve the precision, safety, and efficacy of cell-based therapeutics.

2. Results and Discussion

2.1. Development and Characterization of Peptide Emulsions

To generate the nanoemulsion contrast agent, and facilitate macrophage uptake, we utilize an integrin-targeting peptide emulsifier that self-assembles at the surface of perfluorocarbon (PFC) nanodroplets: $F_FF_FF_F$GGGCCGGKGRGD-NH_2 (hereafter referred to as F_F-RGD, F_F: pentafluorophenylalanine (F_5-Phe), G: glycine, C: cysteine, K: lysine R: arginine, and D: aspartic acid) (Figure S1, Supporting Information).[18,19] The fluorinated *N*-terminus promotes assembly of the peptide at PFC-water interfaces, while two cysteines within the central glycine-rich spacer allow for intermolecular disulfide-crosslinking between adjacent peptides to stabilize the formed particle. Finally, a *C*-terminal RGD motif is displayed from the surface of the emulsion to enable binding with $\alpha_V\beta_3$ integrins highly expressed on the surfaces of macrophages to promote cellular internalization.[20,21]

Next, we utilized varying assembly conditions to generate four distinct morphologies of the nanoemulsions (**Figure 1**a). Using perfluorohexane (PFH) as the PFC droplet template, we began by dispersing the F_F-RGD emulsifier within the fluorous solvent and adding the mixture to water. Spontaneous assembly of the emulsifier at the PFH droplet surface led to the formation of emulsions with a uniform surface monolayer. The resultant particles could then be left non-crosslinked (N-pEM) or further stabilized by oxidizing the cysteine residues in the presence of dimethyl sulfoxide (DMSO) to form disulfide crosslinked particles (pEM). Reversing the formulation procedure produced divergent surface morphologies. For example, dispersing F_F-RGD in water first, before the addition of PFH, generated 1D protofibrils ≈4 nm in width and 38 nm in length (Figure 1b; Figure S2, Supporting Information). This pre-assembly is likely directed by fluorophilic interactions between F_5-Phe residues to sequester the fluorinated block away from the bulk water solvent, generating fibrillar assemblies. Treating the nanofibrils with thioflavin T (ThT), a dye that displays enhanced fluorescence upon binding to amyloid structures,[22] suggests these fibrils are β-sheet rich in nature (Figure 1c). Yet, a canonical β-sheet signal was not observed when performing circular dichroism (CD) spectroscopy (Figure 1d), which is expected to yield a minimum centered at ≈216 nm. Instead, we observed a positive peak at 212 nm, unusual given the *L*-chiral nature of this peptide and that *D*-chirality is typically required to produce positive CD ellipticities.[23] Careful review of the literature suggests this CD feature can be attributed to $n\rightarrow\pi^*$ transitions that occur due to stacking of aromatic groups within the assembling F_5-Phe residues.[24]

To further investigate this unusual CD profile, and specifically isolate fluorine-fluorine driven effects, we synthesized an analogous sequence (F-RGD) containing natural, non-fluorinated, Phe residues (Figure S3, Supporting Information). We observed a similar CD spectrum to F_F-RGD, with the exception that the positive peak was redshifted by 7 nm (Figure S4a, Supporting Information); likely due to the absence of fluorine-driven aggregation. Although CD profiles between the two peptides were similar, TEM analysis showed F-RGD assembly produced long, highly persistent fibrils, several microns in length (Figure S4b, Supporting Information). Interestingly, emulsification using the non-fluorinated F-RGD peptides also did not yield stable emulsions (Figure S5, Supporting Information), suggesting the immiscibility of natural Phe residues in the fluorous solvent prevented their interfacial assembly. With this in mind, we focused our attention on F_F-RGD and found that disulfide crosslinking of F_F-RGD nanofibrils in the presence of DMSO generated ordered 2D sheets (Figure 1e). These sheets displayed reduced amyloid signals relative to the fibrils (Figure 1c), possibly due to a more crowded intermolecular arrangement that inhibited intercalation of the ThT dye. Collectively, our data suggest a combination of aromatic and fluorine-fluorine interactions promotes the organization of F_5-Phe into highly rigid 1D fibrillar assemblies in water, which then can be further laminated into 2D sheets via intermolecular thiol crosslinking.

Utilizing these varied peptide assembly morphologies (e.g., non-crosslinked/crosslinked unimolecular monolayers, 1D fibrils, and 2D sheets) we developed four distinct emulsions (Figure 1a). All four formulations produced particles of ≈600 nm in diameter (Figure 1f). However, 1D-pEM and 2D-pEM yielded narrower particle size distributions and more opaque solutions, indicative of higher particle yield (Figure S6, Supporting Information), relative to N-pEM and pEM. This may be because 1D-pEM and 2D-pEM are formed via accumulation of solid particulates at the fluorous-water interface, a structure known as a Pickering emulsion,[25] while N-pEM and pEM are stabilized by monomeric surfactants. Prior studies suggest that solid particles irreversibly adsorb to oil-water interfaces and generate more stable emulsions compared to monomeric surfactants,[26] the latter being in dynamic equilibrium between bulk solvation and interfacial organization.[27] Finally, TEM and cryo-SEM imaging enabled visualization of the final emulsion structure for all four formulations (Figure 1g–j; additional images in Figures S7 and S8, Supporting Information).

2.2. Acoustic Activation and Stability

We next investigated how the varied surface morphologies of the F_F-RGD emulsion phenotypes influenced their acoustic sensitivity (**Figure 2**a–c; Figure S9, Supporting Information). For these studies, perfluoropentane (PFP) was selected as the fluorous core due to its decreased vaporization point (T_B = 29 °C) relative to PFH (T_B = 56 °C). This allows for lower US energies to be used to induce liquid-to-gas transitions and cause acoustic vaporization,[28] thereby minimizing the potential for acoustic damage to tissues in future applications. Results show that all four emulsion formulations were readily activated at low US intensities (0.1–0.5 W cm^{-2}), achieving ≈40–65% droplet vaporization (**Figure 2**a). Above 1 W cm^{-2}, up to 85% activation was achieved. Vaporization of the emulsions was further confirmed by optical (Figure 2b,c) and fluorescence microscopy (Figure 2d,e), which was limited to micron-sized emulsions due to magnification limitations. For fluorescence visualization, the

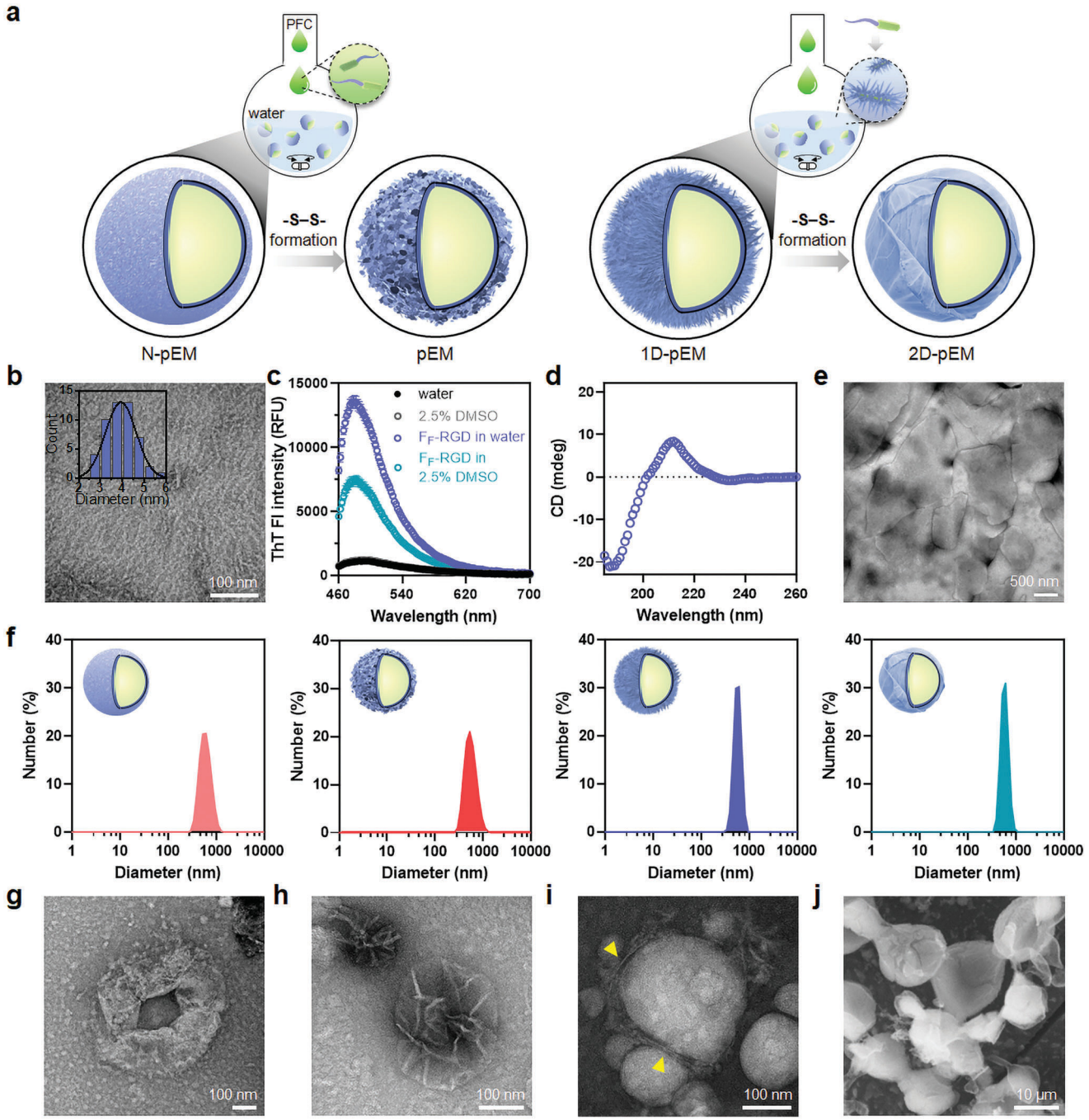

Figure 1. Characterization of F_F-RGD peptide emulsions. a) Schematic representation of peptide emulsions formulated using non-crosslinked (N-pEM) or crosslinked (pEM) peptide monomers, 1D fibrils (1D-pEM) or 2D sheets (2D-pEM). b) Negatively stained TEM image of F_F-RGD nanofibrils; inset shows histogram of fibrillar diameter ($n = 50$). c) ThT fluorescence emission spectra in the presence of F_F-RGD in water (1D fibrils, blue) or in 2.5% DMSO (2D sheets, green) ($n = 3$); $\lambda_{ex} = 430$ nm. [ThT] = 50 µM, [F_F-RGD] = 0.2 mM. d) CD spectrum of F_F-RGD in water, [F_F-RGD] = 0.2 mM. e) Negatively stained TEM image of 2D F_F-RGD sheets. f) Size distribution of the fluorous emulsions; N-pEM, pEM, 1D-pEM, and 2D-pEM (from left to right). Negatively stained TEM images of g) N-pEM, h) pEM, and i) 1D-pEM. j) Cryo-SEM image of 2D-pEM. Yellow arrows in panel (i) denote fibrils adsorbed on the surface of the PFC droplet.

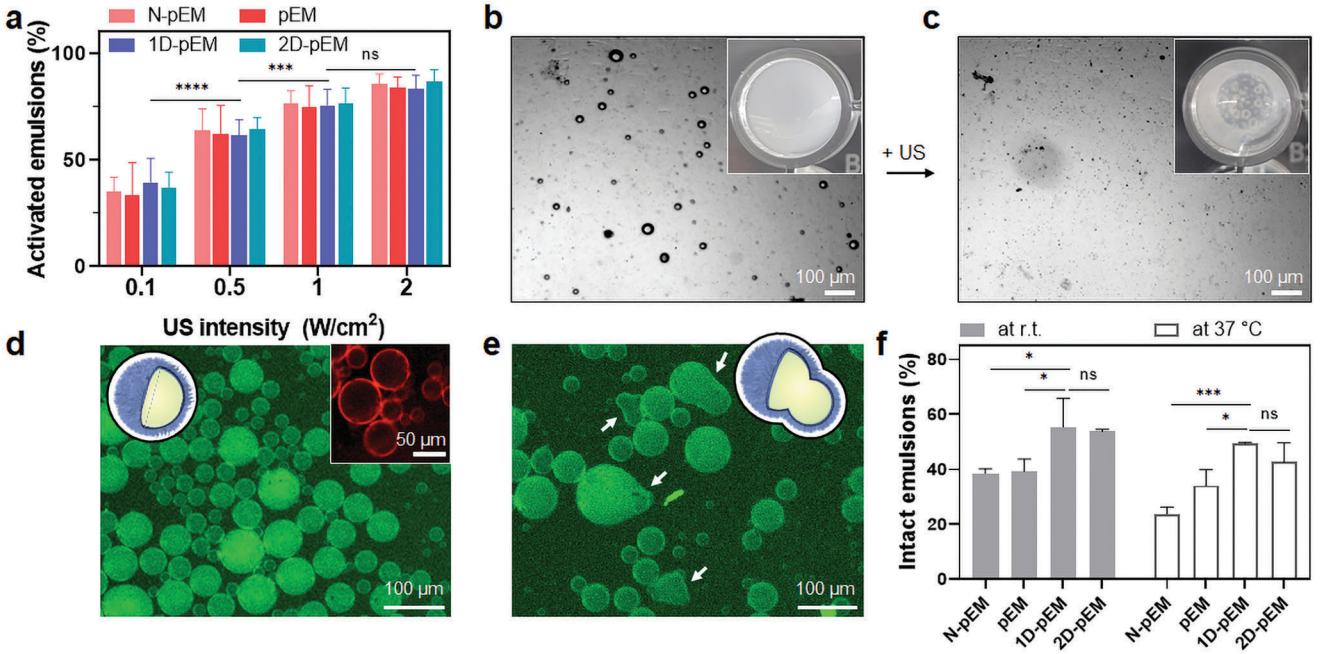

Figure 2. US-activation and stability of PFP-based F_F-RGD emulsions. a) Percentage of emulsions vaporized (activated) following insonation at 37 °C under varying US intensities (1 MHz; 0.1–2 W cm^{-2}, 50% duty cycle ; 90 s exposure). Statistical analysis was conducted by one-way ANOVA; $n = 5$, $^{****}p < 0.0001$, $^{***}p = 0.0001$, ns: not significant. Optical images of 1D-pEM b) before and c) after insonation (2 W cm^{-2}; 50% duty cycle; 90 s exposure). Insets show a decrease in opacity of the 1D-pEM upon US-treatment, and formation of coalesced bubbles, indicative of emulsion vaporization. d,e) Epifluoroscence micrographs of Nile red-loaded 1D-pEM particles d) before and e) after exposure to US (1 W cm^{-2}; 50% duty cycle; 90 s exposure). Inset of (d) shows accumulation of Nile red at the PFP-water interface where F_F-RGD fibrils are located. White arrows in panel (e) denote coalescence of 1D-pEMs that have recondensed after vaporization. f) Stability of the emulsions after incubation either at room temperature (r.t.) or at 37 °C for 24 h. Statistical analysis was conducted by one-way ANOVA; $n = 3$, $^{*}p < 0.05$, $^{***}p < 0.0005$, ns: not significant.

hydrophobic dye Nile red was loaded into the liquid interior of 1D-pEM emulsions. Interestingly, we found that Nile red dissolved within the PFP emulsion core had a blueshifted emission spectra, resulting in green fluorescence, while the dye localized at the surface of the particles was characteristically red (see inset of Figure 2d). These spectral shifts are explained by the varied solvatochromic properties of Nile red based on the polarity of the bulk solution.[29] We observed an additional slight blue shift in Nile red's emission spectra upon interaction with F_F-RGD fibrils assembled at the surface of 1D-pEM and 2D-pEM formulations relative to the monolayer particles, likely due to the difference in assembled structures (Figure S10, Supporting Information). Fortunately, these divergent spectral phenomena allow us to independently monitor the dynamics of both the emulsion core and surface assemblies. Microscopy images shown in Figure 2d demonstrate that, before sonication, 1D-pEM emulsions are intact and do not show signs of coalescence. However, after US exposure (1 W cm^{-2}, 90 s) the particle density is reduced, indicating vaporization (Figure 2e). We also observed occasional droplet coalescence, which may result from recondensation of vaporized bubbles back into fused liquid emulsions. Due to the inverse relationship between particle size and acoustic vaporization power,[30,18] these larger coalesced particles would be more readily vaporized on subsequent US exposures. As will be shown later, this emulsion recycling is believed to play a role in the persistence of contrast-enhancing microbubble nuclei for continuous and long-term acoustic imaging.

Finally, we measured the stability of emulsions at room temperature and 37 °C over a 1–4 day incubation period (Figure 2f; Figure S11, Supporting Information). Results show the Pickering emulsions (1D-pEM and 2D-pEM) are generally more stable than their monomeric counterparts (N-pEM and pEM). This can be explained by the irreversible adsorption of solid peptide nanostructures at the PFP-water interface, which provides a strong steric barrier against solvent diffusion and particle coalescence presonication.[26] However, unexpectedly, 1D-pEM was nominally more stable than 2D-pEM under physiologic conditions. This was surprising given that the 1D-pEM emulsion shell is not stabilized by disulfide crosslinking. As Pickering emulsion stability depends on the shape/morphology of the particles adsorbed at the interface,[31] this counterintuitive result may be explained by more efficient adsorption of the short F_F-RGD nanofibrils to the PFP-water interface relative to the much larger 2D sheets. The varied surface morphologies may also alter the presentation of RGD cell-targeting ligands and consequently affect emulsion uptake into macrophages; an assertion we next test in vitro.

2.3. Macrophage Uptake and Persistance

Prior to studying phagocytosis, biocompatibility of each emulsion formulation was assessed after a 24 h incubation with RAW 264.7 murine macrophages at the highest working concentration of the particles (**Figure 3**a). No significant loss of cell viability

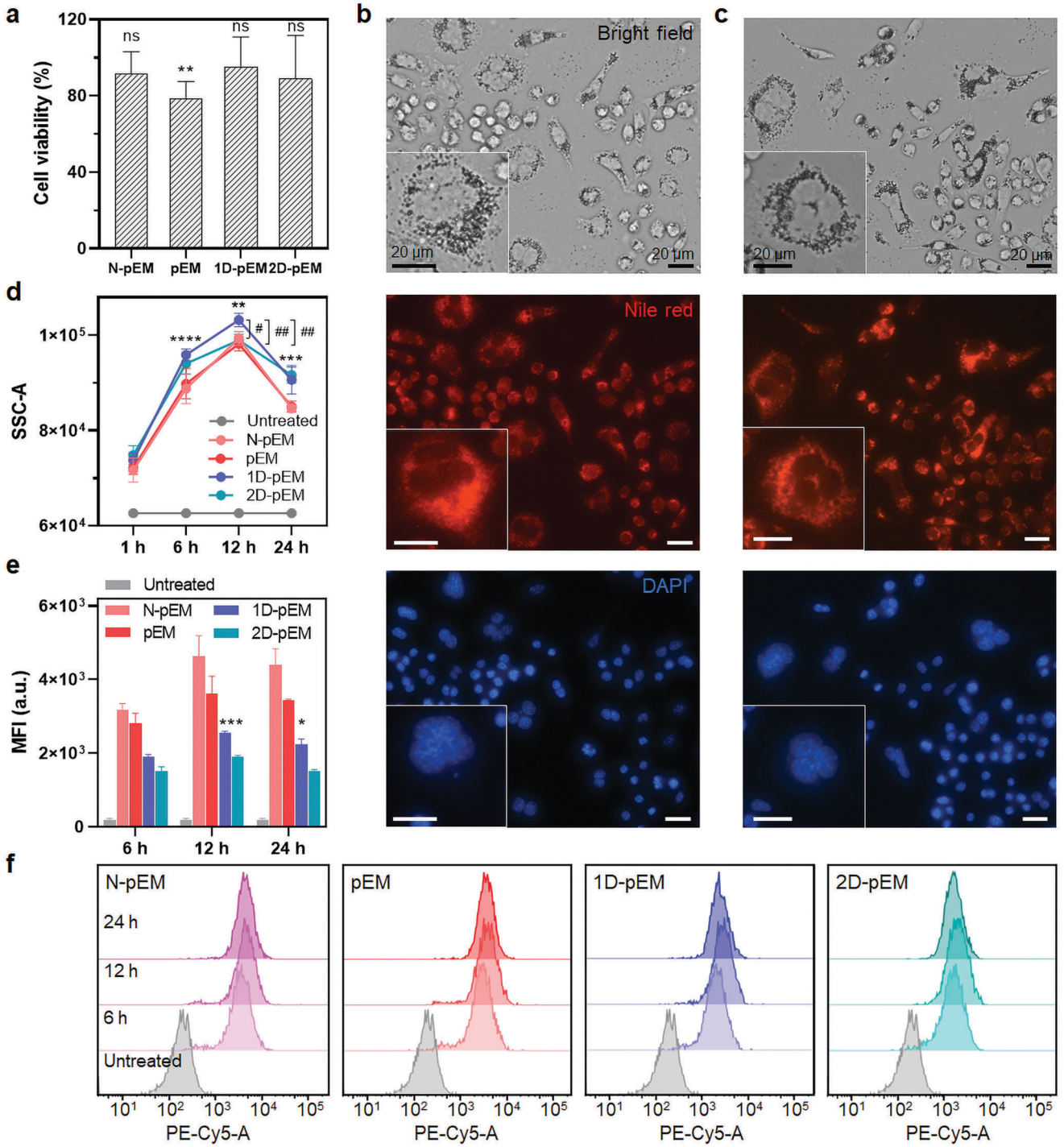

Figure 3. Bioactivity of emulsions within RAW 264.7 macrophages. a) Cell viability measured after 24 h incubation with each emulsion. Statistical analysis was conducted via unpaired *t*-test compared to nontreated control; $n = 10$, ns: not significant, $^{**}p < 0.005$. Epifluorescence micrographs of cells incubated with Nile red-loaded 1D-pEM for b) 6 and c) 24 h. Red fluorescence: Nile red from emulsions and blue fluorescence: DAPI from nuclei. d) Side scattering intensity from macrophages incubated with Nile red-loaded emulsions for each time point. Statistical analyses for 1D-pEM were conducted by one-way ANOVA; $n = 3$, $^{****}p < 0.0001$ between 1 and 6 h, $^{**}p < 0.005$ between 6 and 12 h, $^{***}p < 0.0005$ between 12 and 24 h. $\#p < 0.05$ compared to N-pEM, $\#\#p < 0.01$ compared to pEM and 2D-pEM. e,f) Mean fluorescence intensity (MFI) of Nile red-loaded emulsions in macrophages analyzed by flow cytometry at each time point. Statistical analysis for 1D-pEM in panel (e) was conducted by one-way ANOVA; $n = 3$, $^{***}p < 0.001$ between 6 and 12 h, $^{*}p < 0.05$ between 12 and 24 h.

was observed. With this confirmed we next assessed the time-dependent persistence of Nile red-loaded emulsions in RAW 264.7 cells via epifluorescence microscopy (Figure 3b,c; Figures S12–S14, Supporting Information). Brightfield and fluorescence micrographs taken at 1 h show that emulsions are rapidly internalized into macrophages (Figure S12, Supporting Information), and peak in intracellular load at 12 h of incubation, as confirmed by flow cytometry (Figure 3d-f). The particles subsequently persist within the cells for >3 days (Figure S14, Supporting Information). It is worth noting that, depending on the analysis method used, significant differences in performance between the emulsions are observed. For example, interpreting the side scattering data, which provides a representation of internal cellular density due to particle localization, indicates that 1D-pEM particles show superior intracellular persistence (Figure 3d). Conversely, measuring Nile red fluorescence (Figure 3e) suggests that the monomeric formulations (N-pEM and pEM) outperform the Pickering emulsions (1D-pEM and 2D-pEM). We believe the side scattering data to be more representative of particle performance given that the instability of the monomeric emulsions (Figure 2f) may lead to premature leakage of the Nile red dye,[32] and consequently exaggerated cellular fluorescence results. The superior internalization and persistence of 1D-pEM emulsions may be explained by a combination of factors. First, 1D-pEM showed the greatest stability at physiological temperature compared to the other three formulations (Figure 2f; Figure S11, Supporting Information). Additionally, the fibrillar assembly of F_F-RGD peptides may make it both resistant to proteolytic degradation[33] and able to multivalently display RGD peptide motifs at the particle surface to maximize interactions with the $\alpha_v\beta_3$ receptor on the macrophages.[34]

Based on the dense intracellular accumulation of particles we next evaluated whether US-induced emulsion vaporization would compromise macrophage cell viability. To study this, RAW 264.7 cells were incubated with 1D-pEM for 12 h, followed by treatment with 1 MHz US at different intensities. We observed no significant change in viability for cells with internal vaporization of 1D-pEM compared to controls exposed to US alone (Figure S15, Supporting Information). The ability of these cells to tolerate intracellular generation of cavitating bubbles may be due to the combination of high cytoplasmic viscosity[35] and local crowding by intracellular organelles and other emulsions.[36] Together, this may constrain the size of vaporized microbubbles and thereby create gaseous nuclei that are sufficiently small to prevent intracellular damage, as further evidenced by optical imaging of 1D-pEM treated RAW 264.7 cells after US insonation (Figure S16, Supporting Information).

2.4. In Vitro and Ex Vivo US Imaging of Emulsion-Laden Macrophages

Evaluating the imaging performance of the emulsions was first conducted using high-resolution B-mode in tissue-mimetic agar phantoms. For these studies, pEM, 1D-pEM, and 2D-pEM formulations were prioritized based on their stability and initially evaluated for imaging contrast in the absence of the macrophage host (**Figure 4**a; Figure S17, Supporting Information). Results show the highest contrast is obtained from the 1D-pEM particles, achieving a 2.4-fold enhancement in signal relative to the control of media alone. Given that, among all emulsions tested, 1D-pEM particles show optimal stability (Figure 2f), cellular persistence (Figure 3d), and imaging contrast (Figure 4a), this formulation was prioritized for further investigation of macrophage imaging.

B-mode US imaging of RAW 264.7 cells loaded with 1D-pEM (hereafter referred to as 1D-pEM-RAW) was performed by pretreating cells with the particles for 12 h, loading the contrast-enhanced cells into agar phantoms, and then submerging the sealed phantom into a 37 °C degassed water tank. The vaporization threshold was then measured by gradually increasing the peak positive and negative pressures (Figure 4b,c) until a significant change of contrast was observed. As shown in Figure 4b, B-mode imaging at low negative pressure of 0.3 MPa produced weak US signals due to the majority of emulsions remaining in the liquid phase. Increasing the peak negative pressure to 0.6 MPa induced a liquid-to-gas phase transition that generated echogenic microbubbles within the cells, yielding a significant enhancement in 1D-pEM-RAW cell contrast (Figure 4c). Similar studies in blood indicated that, although background echogenicity is increased, 1D-pEM-RAW cells could still be clearly resolved from the noise (Figure S18, Supporting Information). In some cells, a sufficient number of intracellular microbubbles were created to cause the macrophages to become buoyant and float to the media surface (Movie S1, Supporting Information). It is possible that, once outside of the imaging field, these cells may lose their buoyancy as the bubbles collapse or recondense back into liquid emulsions. Importantly, the mechanical index (0.14 at P− = 0.6 MPa), the spatial peak temporal average intensity (8 mW cm^{-2} at P+ = 1.1 MPa), and the spatial peak pulse average intensity (10 W cm^{-2} at P+ = 1.1 MPa) required to generate high contrast B-mode images of 1D-pEM-RAW are all below the FDA diagnostic limit of 1.9, 720 mW cm^{-2}, and 190 W cm^{-2}, respectively,[37] demonstrating the safety and translatability of this platform.

Next, to evaluate the persistence of imaging contrast during long-term US surveillance, the B-mode intensity of 1D-pEM-RAW cells was monitored over a 60 min continuous insonation period (Figure 4d–f; Figure S19, Supporting Information). Remarkably, we did not observe a statistically significant attenuation in the signal over the entire 1 h imaging time. This is in stark contrast to conventional microbubbles that have imaging half-lives of ≈2–20 min.[38,39] These findings suggest that the low negative acoustic pressure (0.4 MPa) used to induce vaporization of our emulsions permits stable bubble oscillation, as opposed to explosive cavitation, to provide persistent contrast without inducing macrophage damage.[40] Together, this demonstrates the feasibility of prolonged and repeated US imaging of emulsion-loaded macrophages with high spatiotemporal resolution.

To further validate this platform in tissues we assessed the real-time imaging performance of 1D-pEM-RAW cells circulating within the vasculature of a porcine heart, or unloaded cells as control (**Figure 5**; Figure S20, Supporting Information). Here, the coronary artery was catheterized, and a degassed glycerol solution loaded with 1D-pEM-RAW cells was injected via a syringe pump at a flow rate of 1 mL min^{-1}. Contrary to the control (Figure S20a and Movie S3, Supporting Information), contrast enhanced

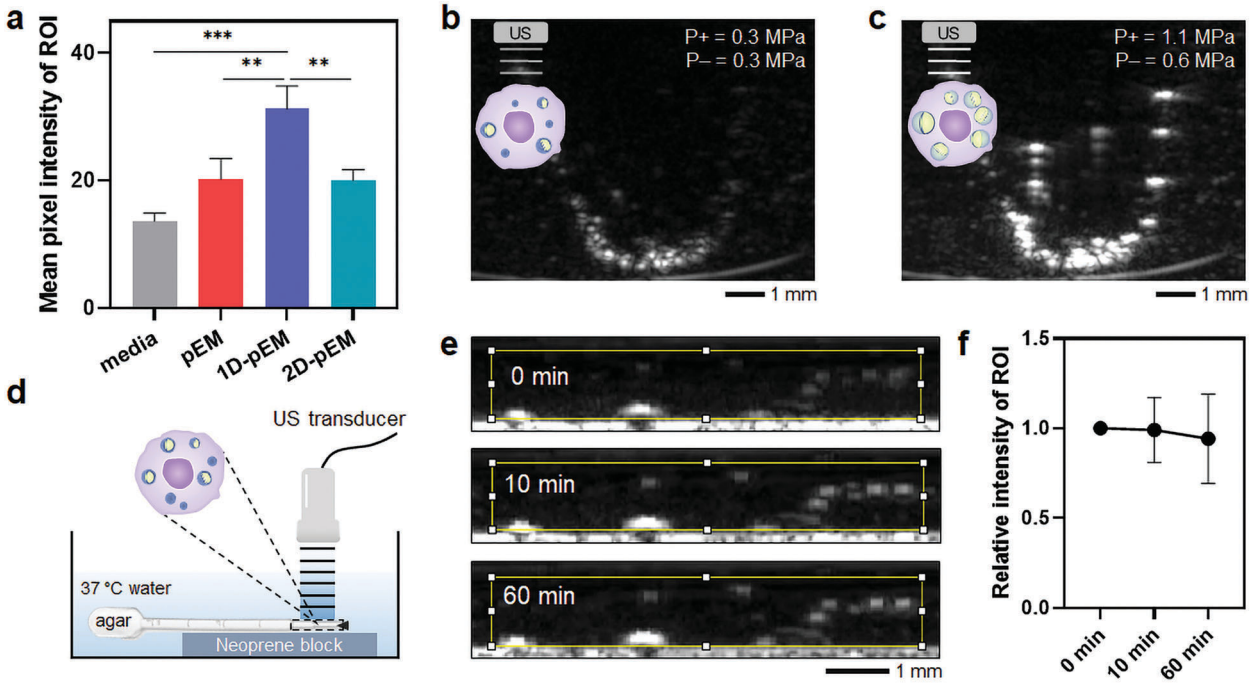

Figure 4. In vitro US imaging. a) Comparison of pEM, 1D-pEM, and 2D-pEM emulsion B-mode echogenicity relative to blank media. Region of interest (ROI) mean pixel intensity was measured from greyscale B-mode images (18 MHz, P+ = 0.5 MPa, P– = 0.4 MPa, one cycle). Statistical analysis was conducted by one-way ANOVA; $n = 3$, $^{***}p = 0.0002$, $^{**}p < 0.005$. b,c) Representative B-mode image of agar phantom loaded with 1D-pEM-RAW cells and insonated at acoustic pressures of b) P+ = 0.3 MPa, P– = 0.3 MPa, and c) P+ = 1.1 MPa, P– = 0.6 MPa (see video in Movie S1, Supporting Information). d) Experimental setup for measuring time-dependent B-mode contrast of 1D-pEM-RAW cells. e) Representative B-mode images of 1D-pEM-RAW cells at varying exposure times (18 MHz, P+ = 0.5 MPa, P– = 0.4 MPa, one cycle). Yellow rectangle defines ROI used for quantification. f) Relative pixel intensity of 1D-pEM-RAW B-mode images (ROI in panel e) over the 60 min insonation period ($n = 3$).

1D-pEM-RAW cells were clearly visualized under B-mode imaging as they perfused through the vessel, allowing single cell tracking and monitoring (see colored circles in Figure 5b). Quantification of the B-mode signal demonstrated a 4.7-fold increase in the contrast of 1D-pEM-RAW cells relative to the tissue background (Figure 5c). In separate experiments, color Doppler US (5 MHz) was employed to evaluate the potential of this modality to further improve the spatiotemporal resolution of 1D-pEM-RAW cell imaging (Figure 5d). Here, a frequency shift in the acoustic signal reflected from the surface of oscillating bubbles is interpreted by the US transducer to provide a colored feature that enables clearer differentiation of the contrast nuclei from the surrounding tissue. As shown in Figure 5d, and Movie S4 (Supporting Information), Doppler signals were observed throughout the vessel during perfusion with 1D-pEM-RAW cells. We ascribe these color features to the circulating 1D-pEM-RAW cells since control vessels perfused with unloaded cells did not show similar signals (Figure S20b and Movie S5, Supporting Information), and separate experiments demonstrated that free emulsions themselves provide strong Doppler contrast during stable oscillation in agar (Figure S21 and Movie S6, Supporting Information). These findings are further validated from prior studies that report microbubbles phagocytosed by leukocytes produce a higher mean frequency echo relative to free bubbles due to intracellular viscous dampening.[40] While additional studies are needed to comprehensively validate this assertion, the early results reported here substantiate the ability of peptide nanoemulsions to enable contrast-enhanced in situ US imaging of macrophages in a real-time, continuous, and precise manner.

3. Conclusion

Macrophages are attractive immune cells as they can be leveraged and engineered for diagnostic and therapeutic purposes. Accordingly, real-time and non-invasive monitoring of these cells with spatiotemporal resolution will improve patient outcomes during treatment with adoptive or allogenic products and may reveal previously unknown activities of macrophages during disease progression. As we show here, phase-changing nanoemulsions that can be acoustically activated to form bubble-based nuclei within macrophages enable in situ imaging of these cells using traditional diagnostic US modalities. This advance is made possible by controlling the assembly pathway of the fluorinated peptide emulsifier at the droplet surface, ultimately leading to formulations that are efficiently internalized into macrophages and stably oscillate under B-mode and Doppler US imaging. A noteworthy advantage of our peptide emulsifiers, relative to traditional lipids and polymers, is that their sequences can be readily tuned to possess varying cross-linking moieties and cell-targeting motifs, without the necessity of secondary chemical modification. As a result, emulsifying peptides can be rationally designed to target a range of cell-types for application-specific requirements, while exploiting the synthetic tractability of solid-phase synthesis techniques. However, peptides also have pharmacologic lia-

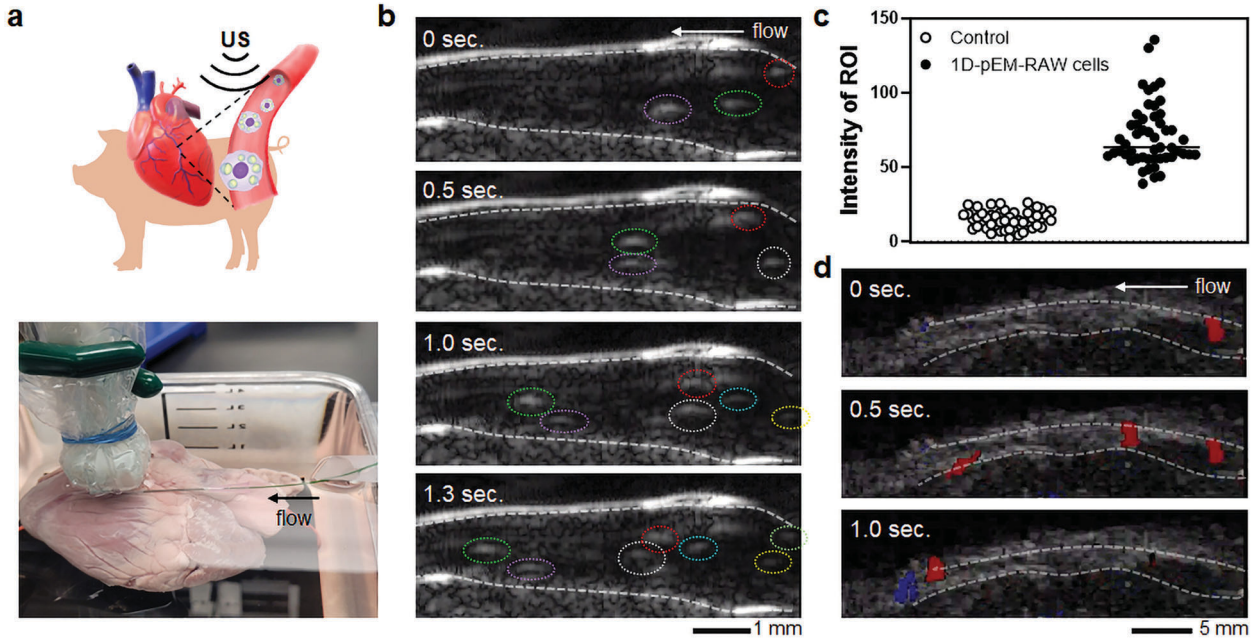

Figure 5. Real-time monitoring of emulsion-laden RAW 264.7 cells within tissues. a) Top: schematic illustration of US macrophage tracking within porcine vasculature. Bottom: photograph of ex vivo experimental setup for B-mode US imaging in the catheterized porcine coronary artery. b) Representative time-dependent B-mode images (18 MHz, P+ = 0.5 MPa, P− = 0.4 MPa) of 1D-pEM-RAW cells during vessel perfusion (see full video in Movie S2, Supporting Information). Vessel walls are demarcated by white dashed lines. Colored dashed circles track individual 1D-pEM-RAW cells during flow. c) Quantification of B-mode contrast for 1D-pEM-RAW cells compared to background controls (n = 50 each; unpaired t-test was performed between conditions, with $p < 0.0001$). d) Color Doppler signals (5 MHz, P+ = 4.1 MPa, P− = 1.8 MPa), superimposed on B-mode images collected during 1D-pEM-RAW cell vessel perfusion (see full video in Movie S4, Supporting Information). White arrows in panel (b) and (d) represent flow direction.

bilities that lipids and polymers do not, particularly proteolytic degradation. Therefore, further preclinical work is necessary to fully characterize the in vivo stability, persistence, and performance of these contrast agents. Nevertheless, we believe this platform is poised to open new diagnostic opportunities for real-time monitoring, guidance, and manipulation of macrophage distribution and behavior in tissues. As clinically relevant examples, such capabilities would allow for better management of adoptive CAR-macrophage immunotherapies and enable in situ investigation of macrophage activity during pathogenesis. In sum, this technology has the potential to nucleate the design of a broad array of US-controlled nanoscale tools that can impact diverse areas in biotherapeutic discovery and immunobiology, all while leveraging the portable, non-invasive, and safe nature of diagnostic US.

Supporting Information

Supporting Information is available from the Wiley Online Library or from the author.

Acknowledgements

Transmission and scanning electron microscopy, and flow cytometry were performed at the Penn State Microscopy and Cytometry Facility, University Park, PA. In particular, the authors would like to acknowledge John Cantolina from the Huck Institutes at Pennsylvania State University for assistance with cryogenic scanning electron microscopy. The authors also acknowledge the Penn State Materials Characterization Laboratory for use of the dynamic light scattering instrumentation. Funding for this work was provided by NSF DMR-1845053, NIH R35-GM142902, and NIH R21-DK128638 awarded to S.H.M. Porcine hearts were obtained as remnant tissue from a local slaughterhouse, and not subject to IACUC regulation. Informed written consent was obtained prior to research using human specimans collected under IRB #00012449.

Conflict of Interest

The authors declare no conflict of interest.

Data Availability Statement

The data that support the findings of this study are available from the corresponding author upon reasonable request.

Keywords

fluorine, macrophage, peptide, self-assembly, ultrasound

Received: February 24, 2023
Revised: June 22, 2023
Published online: July 14, 2023

[1] T. A. Wynn, A. Chawla, J. W. Pollard, *Nature* **2013**, *496*, 445.
[2] D. Hirayama, T. Iida, H. Nakase, *Int. J. Mol. Sci.* **2018**, *19*, 92.
[3] T. J. Koh, L. A. DiPietro, *Expert Rev. Mol. Med.* **2011**, *13*, e23.

[4] T. A. Wynn, K. M. Vannella, *Immunity* **2016**, *44*, 450.
[5] J. M. Olefsky, C. K. Glass, *Annu. Rev. Physiol.* **2010**, *72*, 219.
[6] K. J. Moore, F. J. Sheedy, E. A. Fisher, *Nat. Rev. Immunol.* **2013**, *13*, 709.
[7] R. W. Kinne, R. Bräuer, B. Stuhlmüller, E. Palombo-Kinne, G.-R. Burmester, *Arthritis Res.* **2000**, *2*, 189.
[8] Y. Xia, L. Rao, H. Yao, Z. Wang, P. Ning, X. Chen, *Adv. Mater.* **2020**, *32*, 2002054.
[9] A. Mantovani, P. Allavena, F. Marchesi, C. Garlanda, *Nat. Rev. Drug Discovery* **2022**, *21*, 799.
[10] S. Lee, S. Kivimäe, A. Dolor, F. C. Szoka, *J. Controlled Release* **2016**, *240*, 527.
[11] A. Faucon, H. Benhelli-Mokrani, L. A. Córdova, B. Brulin, D. Heymann, P. Hulin, S. Nedellec, E. Ishow, *Adv. Healthcare Mater.* **2015**, *4*, 2727.
[12] S. Temme, F. Bönner, J. Schrader, U. Flögel, *WIREs Nanomed. Nanobiotechnol.* **2012**, *4*, 329.
[13] C. C. Parker, S. E. Lapi, *Cancers* **2021**, *13*, 1921.
[14] P. A. Dayton, J. J. Rychak, *Front. Biosci.* **2007**, *12*, 5124.
[15] H. Yusefi, B. Helfield, *Front. Phys.* **2022**, *10*, 791145.
[16] M. Ahmed, B. Cerroni, A. Razuvaev, J. Härmark, G. Paradossi, K. Caidahl, B. Gustafsson, *Cell. Mol. Bioeng.* **2017**, *10*, 537.
[17] S. Garg, A. A. Thomas, M. A. Borden, *Biomaterials* **2013**, *34*, 6862.
[18] S. H. Medina, M. S. Michie, S. E. Miller, M. J. Schnermann, J. P. Schneider, *Angew. Chem., Int. Ed.* **2017**, *56*, 11404.
[19] J. N. Sloand, T. T. Nguyen, S. A. Zinck, E. C. Cook, T. J. Zimudzi, S. A. Showalter, A. B. Glick, J. C. Simon, S. H. Medina, *ACS Nano* **2020**, *14*, 4061.
[20] R. Hanayama, M. Tanaka, K. Miwa, A. Shinohara, A. Iwamatsu, S. Nagata, *Nature* **2002**, *417*, 182.
[21] A. S. Antonov, G. N. Antonova, D. H. Munn, N. Mivechi, R. Lucas, J. D. Catravas, A. D. Verin, *J. Cell. Physiol.* **2011**, *226*, 469.
[22] M. Biancalana, S. Koide, *Biochim. Biophys. Acta* **2010**, *1804*, 1405.
[23] T. M. Clover, C. L. O'Neill, R. Appavu, G. Lokhande, A. K. Gaharwar, A. E. Posey, M. A. White, J. S. Rudra, *J. Am. Chem. Soc.* **2020**, *142*, 19809.
[24] D. M. Ryan, T. M. Doran, S. B. Anderson, B. L. Nilsson, *Langmuir* **2011**, *27*, 4029.
[25] S. Bai, C. Pappas, S. Debnath, P. W. J. M. Frederix, J. Leckie, S. Fleming, R. V. Ulijn, *ACS Nano* **2014**, *8*, 7005.
[26] R. Aveyard, B. P. Binks, J. H. Clint, *Adv. Colloid Interface Sci.* **2003**, *100–102*, 503.
[27] Z. Zhao, W. Wang, J. Xiao, Y. Chen, Y. Cao, *Nanomaterials* **2020**, *10*, 1068.
[28] M. L. Fabiilli, K. J. Haworth, N. H. Fakhri, O. D. Kripfgans, P. L. Carson, J. B. Fowlkes, *IEEE Trans. Ultrason., Ferroelect., Freq. Contr.* **2009**, *56*, 1006.
[29] P. Greenspan, S. D. Fowler, *J. Lipid Res.* **1985**, *26*, 781.
[30] P. S. Sheeran, S. H. Luois, L. B. Mullin, T. O. Matsunaga, P. A. Dayton, *Biomaterials* **2012**, *33*, 3262.
[31] D. G. Ortiz, C. Pochat-Bohatier, J. Cambedouzou, M. Bechelany, P. Miele, *Engineering* **2020**, *6*, 468.
[32] M. Pan, L. Rosenfeld, M. Kim, M. Xu, E. Lin, R. Derda, S. K. Y. Tang, *ACS Appl. Mater. Interfaces* **2014**, *6*, 21446.
[33] A. P. Blum, J. K. Kammeyer, J. Yin, D. T. Crystal, A. M. Rush, M. K. Gilson, N. C. Gianneschi, *J. Am. Chem. Soc.* **2014**, *136*, 15422.
[34] M. Dzuricky, S. Xiong, P. Weber, A. Chilkoti, *Nano Lett.* **2019**, *19*, 6124.
[35] J. R. Lindner, P. A. Dayton, M. P. Coggins, K. Ley, J. Song, K. Ferrara, S. Kaul, *Circulation* **2000**, *102*, 531.
[36] S.-T. Kang, C.-K. Yeh, *Langmuir* **2011**, *27*, 13183.
[37] T. R. Nelson, J. B. Fowlkes, J. S. Abramowicz, C. C. Church, *J. Ultrasound Med.* **2009**, *28*, 139.
[38] R. Song, C. Peng, X. Xu, J. Wang, M. Yu, Y. Hou, R. Zou, S. Yao, *ACS Appl. Mater. Interfaces* **2018**, *10*, 14312.
[39] J. Cen, X. Ye, X. Liu, W. Pan, L. Zhang, G. Zhang, N. He, A. Shen, J. Hu, S. Liu, *Angew. Chem.* **2022**, *134*, e202209610.
[40] P. A. Dayton, J. E. Chomas, A. F. H. Lum, J. S. Allen, J. R. Lindner, S. I. Simon, K. W. Ferrara, *Biophys. J.* **2001**, *80*, 1547.